Experimental and Numerical Studies of Densification and Grain Growth of 8YSZ during Flash Sintering

Shufan Wang,* Tarini Prasad Mishra, Yuanbin Deng, Anke Kaletsch, Martin Bram, and Christoph Broeckmann

As a promising sintering technique, flash sintering utilizes high electric fields to achieve rapid densification at low furnace temperatures. Various factors can influence the densification rate during flash sintering, such as ultrahigh heating rates, extra-high sample temperatures, and electric field. However, the determining factor of the densification rate and the key mechanism during densification are still under debate. Herein, the densification and grain growth kinetic during flash sintering of 8 mol% Y_2O_3-stabilized ZrO_2 (8YSZ) is studied experimentally and numerically using finite element method (FEM). The roles of Joule heating and heating rate on the densification are investigated by comparing flash sintering with conventional sintering. An apparently smaller activation energy for the material transport resulting in densification is obtained by flash sintering ($Q_d = 424$ kJ mol^{-1}) compared to the conventional sintering ($Q_d = 691$ kJ mol^{-1}). In addition, a constitutive model is implemented to study both the densification and the grain growth during flash and conventional sintering. Furthermore, the effect of electrical polarity on the density and the grain size evolution during flash sintering of 8YSZ is also investigated. The simulation results of average density and grain size inhomogeneity agree well with the experimental data.

S. Wang, Y. Deng, A. Kaletsch, C. Broeckmann
Institute of Applied Powder Metallurgy and Ceramics at RWTH Aachen e.V. (IAPK)
Augustinerbach 4, 52062 Aachen, Germany
E-mail: s.wang@iwm.rwth-aachen.de

T. P. Mishra, M. Bram
Forschungszentrum Jülich GmbH
Institute of Energy and Climate Research: Materials Synthesis and Processing (IEK-1)
52425 Jülich, Germany

Y. Deng, A. Kaletsch, C. Broeckmann
Institute for Materials Applications in Mechanical Engineering (IWM)
RWTH Aachen University
Augustinerbach 4, 52062 Aachen, Germany

M. Bram
Ruhr-Universität Bochum
Institut für Werkstoffe
Universitätsstraße 150, 44801 Bochum, Germany

The ORCID identification number(s) for the author(s) of this article can be found under https://doi.org/10.1002/adem.202201744.

1. Introduction

Flash sintering has drawn wide research attentions since the first publication on flash sintered 3 mol% yttria-stabilized zirconia (3YSZ) in 2010[1,2] due to the significant reduction of time and temperature required for the ceramic densification. In a typical flash sintering experiment, an electric field is directly applied to the green sample so that the current flows within the body at a certain furnace temperature. The onset of flash sintering is characterized by a nonlinear increase in conductivity concurrent with an abrupt heat dissipation and fast densification.[3–5] Recent studies focused mostly on the understanding of the underlying densification mechanisms during flash sintering. Various influencing factors contribute to the rapid densification, such as internally generated Joule heating by thermal runaway,[3,6,7] grain boundary overheating with local melting,[8–10] extremely high heating rates,[11,12] and formation of defects such as oxygen vacancies[13,14] or Frenkel pairs.[15,16] However, to what extent the nonthermal (electric field) factor is engaged in the enhanced densification is still not fully understood.

The influence of electric field on the sintering process has been studied for various oxide ceramic materials, including zinc oxide,[17,18] alumina,[19] gadolinium doped ceria (GDC),[20,21] and yttria-stabilized zirconia (YSZ).[22–25] Schmerbauch et al.[17] studied the flash sintering behavior of nanocrystalline zinc oxide using noncontacting electrodes to avoid current flow and the resulting Joule heating. They observed the enhanced densification and coarsening of ZnO even in the absence of electric current flowing through the sample. Cao et al.[26] measured the viscosity and sintering stress under different electrical potentials experimentally using a loading dilatometry. It was revealed that moderate alternating current (AC) electric fields can decrease the uniaxial viscosity and increase the sintering stress of yttria-doped ceria (YDC). In addition, molecular dynamics (MD) simulations have been carried out by Xu et al.[23] to calculate the diffusion coefficients of Y, Zr, and O ions in the 8 mol% yttria-stabilized zirconia (8YSZ) system under electric field; the results show that an intense electric field promotes the formation of cation Frenkel pair defects and enhances the diffusivities of cations and anions in the 8YSZ system. Apart from the effect of electric field on

densification, asymmetrical microstructure caused by electrical polarity has also been widely observed in flash sintering as well as field-assisted sintering technology/spark plasma sintering (FAST/SPS).[18,20–22,24,25,27,28] However, the results regarding grain growth in favor of a particular electrode side and the reasons for inhomogeneity vary from material to material.[29]

On the other hand, many researchers tried to explain the abrupt densification during flash sintering only from the thermal aspect.[12,24,30] In their works, the enhanced densification was attributed to the altered mass transport mechanism caused by the ultrahigh heating rate in flash sintering. Very early studies of heating rate on the sintering behavior were conducted by Johnson et al.[31–33] It was found that very fast densification with small grain sizes of alumina can be achieved by fast firing. The study of heating rate effect on the densification of ZnO during flash sintering was reported by Zhang et al.[30]. In their works, the rapid thermal annealing (RTA) experiments were conducted to mimic the heating profiles in flash sintering. It was observed that RTA experiments achieved similar densification and grain growth rates of the ZnO samples as those in flash sintering. Moreover, Ji et al.[12] compared different fast firing techniques with flash sintering on the example of 3YSZ. It was concluded that rapid heating ($>6000 \, \text{K} \, \text{min}^{-1}$) without electric field can accelerate the sintering process of 3YSZ by over two orders of magnitude compared with conventional heating ($5 \, \text{K} \, \text{min}^{-1}$) to the same temperature. This reveals that the primary reason for abrupt densification in flash sintering of 3YSZ is the ultrafast Joule heating rather than a direct influence of the electric field or a higher maximum temperature than normal sintering temperature. Furthermore, Ji et al.[34] investigated the microstructural development of 3YSZ during ultrafast firing and found that rapid heating methods resulted in smaller pores than conventional heating, which contributed to the acceleration of densification. Recently, Bhandari et al.[24] demonstrated in experiments that the rapid densification in flash sintering of 8YSZ is primarily dominated by Joule heating, whereas the influence of electric field is mainly on the grain growth behavior. In 2020, another novel sintering technique named ultrafast high-temperature sintering (UHS) was introduced by Wang et al.[35] With a comparable heating rate to flash sintering, UHS excludes the effect of electric field on the sintering of ceramic compacts by indirectly heating the sample with the use of graphite felt as a "furnace." Mishra et al.[36] simulated the temperature reached during UHS of $SrTiO_3$ and compared the results with conventional dilatometry sintering. It was found that at similar sintering temperatures for both techniques, UHS significantly accelerated the sintering process. This enhanced densification was attributed to the ultrahigh heating rate of $\approx 10^4 \, \text{K} \, \text{min}^{-1}$.

To investigate the impact of Joule heating on the densification mechanism of flash sintering, the modeling of the electrical–thermal–structural interaction of the ceramic body is needed. Considering the difficulty of the temperature measurement during flash sintering, many researchers have adopted analytical modeling[3,37,38] and finite element methods (FEMs)[4,25,39,40] to calculate the maximum temperature and temperature gradient in the sample. However, very few studies on the modeling of densification during flash sintering were reported till now. Li et al.[41] used FEM coupled with a phenomenological constitutive equation to simulate the densification of flash sintering of 3YSZ.

Arya et al.[42] used the master sintering curve (MSC) to include the influencing factor of the heating rate to predict the densification behavior of 3YSZ, 8YSZ, and TiO_2. Their prediction of relative density (RD) matches closely with the experimental observation at a higher current density (100–150 mA mm^{-2}) while failing at a lower current density (<100 mA mm^{-2}). However, considering the likely changed mass transport mechanism at an ultrahigh heating rate, the validity of extrapolating the experimental data from the conventional heating rate (5–20 K min^{-1}) to ultrahigh heating rate (≈ 2000 K min^{-1}) is questionable. Moreover, both abovementioned works did not incorporate the grain growth factor in the modeling of densification. As the effect of grain size on densification and the ability of ultrahigh heating rate to tailor the microstructure are non-negligible, a sophisticated constitutive model coupled with a grain growth law is urged.

In this work, conventional sintering and flash sintering of 8YSZ were compared by both experimental and numerical methods. Densification and grain growth were studied with the help of FEM with coupled constitutive model and grain growth law.

2. Experimental Section

2.1. Sample Preparation

The starting material was a commercially available granulated 8YSZ powder with a theoretical density of 5.88 g cm^{-3} (Tosoh Corporation, Japan). It had an average particle size of $d_{50} = 0.18 \, \mu\text{m}$ ($d_{10} = 0.08 \, \mu\text{m}$, $d_{90} = 37.26 \, \mu\text{m}$). In this study, two types of green bodies were prepared. For conventional dilatometry sintering, the powder was uniaxially pressed in a cylindrical die at 100 MPa. The pressed samples had a diameter of 8 mm and a height of ≈ 4.5 mm. For flash sintering, 8YSZ powder was uniaxially pressed within a dog-bone-shaped die at 100 MPa. These dog-bone-shaped samples had a gauge length of 15 mm, a width of 3.3 mm, and a thickness of ≈ 2 mm. As the pressed green bodies were too fragile to be connected to the electrodes, they were presintered at 900 °C for 60 min. Both cylinder-shaped and dog-bone-shaped samples had an initial green density of approximately 42–45% measured by the Archimedes method.

2.2. Conventional Sintering

Conventional sintering experiments were carried out in a push rod dilatometer TMA 402 F1 (Netzsch, Germany) in air. 8YSZ green samples were heated up to three sintering temperatures (1200, 1250, and 1300 °C) at a heating rate of 5 K min^{-1}. The dwell time was 2 h for all the experiments. The extracted temperature-shrinkage curves were converted to densification curves using the method described in the work of Maca et al.[43] To study the microstructural evolution, a series of isothermal interrupted sintering experiments were designed. The sintering cycles include a heating rate of 5 K min^{-1}, sintering temperatures between 1300 and 1450 °C with an interval of 50 °C, and dwell times of 0, 12, 30, and 60 min for each sintering temperature. After the sintering experiments, the densities of the sintered samples were measured using the Archimedes method. The samples were thereafter metallographically prepared for the grain size analysis.

2.3. Flash Sintering

The dog-bone-shaped samples were used to conduct the flash sintering experiments. Isothermal flash sintering experiments were carried out at a constant furnace temperature of 850 °C in air. Each sample was placed in the furnace for 15 min before a constant electric field of 100 V cm^{-1} was applied. After the flash event, the device was switched from voltage control to current control, with the current densities ranging from 25 to 125 mA mm^{-2} (in steps of 25 mA mm^{-2}). After holding the sample at each current density for four different dwell times (15, 30, 60, and 120 s), the power supply was turned off. The experimental setup for flash sintering is similar to that shown in the work of Cologna and Raj,[44] and the detailed procedure was described in the work of Bhandari et al.[24] After the process, the ear sections of the dog-bone-shaped samples were removed; the gauge sections were then characterized regarding the density and the microstructure. **Table 1** summarizes the experimental design for both conventional sintering and flash sintering experiments.

2.4. Microstructure Characterization

After the sintering experiments, the microstructure of the samples of both isothermal interrupted conventional sintering and flash sintering was characterized. The cylinder-shaped samples were polished and thermally etched for 25 min at temperatures of 150 °C lower than the corresponding sintering temperatures. For dog-bone-shaped samples, the gauge sections were first ground to the half of their thicknesses and then polished and thermally etched. As the sintering temperatures were not able to be measured during flash sintering experiments, the etching temperatures for each experiment were set as 150 °C lower than the corresponding simulated maximum temperatures. Simulation procedure will be described in Section 3. Subsequently, gold was sputtered on the polished surface to ensure sufficient conductivity for the scanning electron microscopy (SEM) analysis. For cylinder-shaped samples, two locations near the center of the samples were chosen for the imaging. For dog-bone-shaped samples, to study the electrical polarity effect on the samples during flash sintering,

SEM images were taken at three different positions along the gauge section from the anode side to the cathode side (detailed description can be found in Section 4.1.1). With the micrographs, grain size measurements were performed using the linear intercept method with a dimensionality correction factor of 1.56.[45]

3. Numerical Modeling

3.1. Finite Element Modeling

Finite element modeling is a convenient tool to replicate the experimental observation and to study the interaction between the electrical field, temperature profile, and sintering behavior during flash sintering. In this study, coupled thermal–electrical–structural models were established in the software ABAQUS/Standard (v14, Simulia, Dassault Systèmes). The temperature evolution during flash sintering was first simulated based on the well-known general balance equation.[46,47] The self-integrated equations consider the heat generation due to Joule heating and the heat transfer due to conduction, convection, and radiation. In addition, the material constitutive model was implemented in a user subroutine UMAT of ABAQUS. Subsequently, densification and grain growth were predicted for both conventional sintering and flash sintering.

Material properties of 8YSZ were determined by different standard thermophysical experiments. The thermal expansion coefficient was measured using a horizontal dilatometer (DIL402C). The specific heat capacity was measured by the dynamic differential calorimeter (DSC 404 Pegasus NETZSCH, Germany) and the thermal conductivity by laser flash equipment (LFA 427, NETZSCH, Germany). On the other hand, mechanical properties such as Young's modulus and Poisson's ratio were measured by impulse excitation technique (RFDA, IMCE NV, Belgium), for which an Instron furnace was utilized and assembled with the testing system to perform high-temperature measurement. Except for the thermal conductivity, which was measured in argon to avoid oxidation of graphite, all other properties were measured in air. To get an accurate response of the material during the heating process, all the material parameters were determined as a function of temperature. Additionally, the dependence of the thermal conductivity on RD was also considered in the measurements. For flash sintering, electrical conductivity is an essential parameter because the change of the resistance signals the onset of flash and determines the amount of the produced Joule heating. In this study, the time-evolving current and voltage values were extracted from the log data of corresponding experiments. Therefore, along with the sample geometry, the electrical conductivities can be obtained as time dependent values. The contact resistance between the electrode and the green bodies was not considered in the model, as a generous coating of Pt paste was applied in the holes of dog-bone samples to mitigate the contact resistance.

For conventional sintering, different temperature profiles corresponding to the experimental sintering cycles were set on the sample as boundary conditions, while an initial temperature of 850 °C was set for the dog-bone sample as predefined temperature field for the modeling of flash sintering. To ensure that current flows through the sample, a current load with the value of current density was applied to the interior of one hole and a 0

Table 1. Summary of experimental design for sintering experiments.

Experiment	Sintering condition	Dwell time
Dilatometry sintering (to obtain densification curve)	1200 °C	120 min
	1250 °C	120 min
	1300 °C	120 min
Isothermal interrupted conventional sintering (to characterize grain size)	1300 °C	0, 12, 30, 60 min
	1350 °C	0, 12, 30, 60 min
	1400 °C	0, 12, 30, 60 min
	1450 °C	0, 12, 30, 60 min
Isothermal interrupted flash sintering	25 mA mm^{-2}	15, 30, 60, 120 s
	50 mA mm^{-2}	15, 30, 60, 120 s
	75 mA mm^{-2}	15, 30, 60, 120 s
	100 mA mm^{-2}	15, 30, 60, 120 s
	125 mA mm^{-2}	15, 30, 60, 120 s

ADVANCED
SCIENCE NEWS

www.advancedsciencenews.com

ADVANCED
ENGINEERING
MATERIALS

www.aem-journal.com

electrical potential to the other hole. Current densities were obtained by converting the time-evolving current values which were extracted from the experimental log data to accurately replicate the experimental conditions. Moreover, a radiation heat-transfer interaction property was defined on the surface of the sample. An emissivity coefficient of 0.7 from literature[48–50] was adopted in the numerical studies. The convection coefficient, also known as heat transfer coefficient, was determined by an additional calibration process, which was carried out by comparing the different flash-onset temperatures of 8YSZ under different electric fields between the simulation and experiments.[51] The model and the boundary conditions used in the calibration process were also adapted according to the experimental setup in the work of Yadav and Raj.[51] The 8YSZ powder used in their work is from the same manufacturer as that used in the current study. Therefore, the same material properties were implemented for both the calibration and the subsequent simulation, with the exception of electrical conductivity, which was defined as a function of temperature (up to 800 °C) and taken from the work of Zhang et al.[52] for the calibration process. A convection coefficient of 34 W m^{-2} K^{-1} was found to derive the best consistency and therefore used as an input parameter for the simulation in this study.

3.2. Constitutive Model

Material specific model was built based on the modified Skorohod–Olevsky viscous sintering (SOVS) model combined with a grain growth law. The original model was rooted in the rheological theory of sintering established by Skorohod.[53] Olevsky has modified the model for numerical simulations based on continuum mechanics.[54] Furthermore, Shinagawa[55,56] adopted an Arrhenius-type function of the viscosity and expressed the sintering stress as a function of density and grain size. These modifications make the phenomenological constitutive model suitable to describe the densification mechanism during sintering and easy to implement for numerical simulation of sintering of ceramic powders.[57,58] The constitutive equation for inelastic strain rate is formulated as follows

$$\dot{\varepsilon}_{ij} = \frac{1}{2\eta} \frac{1}{\rho^{2n-1}} \left[\sigma'_{ij} + \delta_{ij} \frac{2}{9f^2} (\sigma_m + \sigma_s) \right] \tag{1}$$

where ρ is the density, $f = 1/(2.5\sqrt{1-\rho})$, η is the shear viscosity of the fully dense material, n is the exponential constant, and σ'_{ij}, σ_m, and σ_s represent the deviatoric stress tensor, the hydrostatic stress, and the sintering stress, respectively. δ_{ij} is the Kronecker delta. The sintering stress σ_s is expressed as

$$\sigma_s = \frac{4\gamma}{\xi G} \rho^{N_s} \left[\frac{\rho(1-\rho_0)}{\rho_0(1-\rho)} \right]^{\frac{1}{3}} \tag{2}$$

where γ is the specific surface energy, ξ is the correction factor for sintering stress, G is the grain size, N_s is the fitting constant, and ρ_0 is the initial RD. The viscosity η is formulated as an Arrhenius-type function

$$\eta = C_{s1} T \exp\left(\frac{C_{s2}}{T} \right) \tag{3}$$

where T is the temperature; C_{s1} and C_{s2} are material constants for viscosity. C_{s2} can be expressed as a function of apparent activation energy for densification Q_d and is given by $C_{s2} = Q_d/R$, where R is the molar gas constant, and Q_d indicates the activation energy for the material transport resulting in densification during sintering.

The rate of density change, $\dot{\rho}$, is defined based on the mass conservation equation and can be expressed by the trace of the strain rate tensor $\dot{\varepsilon}_{kk}$ as follows

$$\dot{\rho} = -\rho \cdot \dot{\varepsilon}_{kk} \tag{4}$$

In addition to densification, grain growth is also an influencing factor of the sintering process. The grain growth law used in this study is shown as below[59,60]

$$G^p - G_0^p = Kt = K_0 t \exp\left(-\frac{Q_g}{RT} \right) \tag{5}$$

where t is the time, K_0 is the pre-exponential constant, Q_g is the activation energy for grain growth, and p is the grain growth exponent. With these constitutive equations and the grain growth law, the model was implemented in the user subroutine UMAT of ABAQUS to predict the densification and grain growth during conventional and flash sintering.

4. Results

4.1. Experimental Results

4.1.1. Sintering Analysis with Microstructural Characterization

Figure 1a shows the shrinkage curves and their corresponding RD curves of dilatometry sintering experiments. It can be seen that the samples sintered at 1300 °C for 2 h achieved almost full densification. The sintering trajectory of 8YSZ can be obtained from the isothermal interrupted conventional sintering experiments by plotting grain size against RD for different sintering temperatures and dwell times (Figure 1b). The number around each colored dot represents the dwell time (min), and the sintering temperatures are distinguished by different colors. It can be deduced from the graph that only neglectable grain growth appears for a RD below 92%, above which the grains start to grow significantly. When the density reaches the maximum and stabilizes, the grains continue to grow with the increase of the dwell time. The evolution of the grain sizes of the samples sintered at 1350 °C with four different dwell times is shown by the micrographs in **Figure 2**.

For flash sintering, the measured densities of flash sintered samples were plotted against current densities in **Figure 3**a. The highest RD is around 95% which was reached at the current density of 100 mA mm^{-2} with the dwell time of 120 s, as well as at 125 mA mm^{-2} for all dwell times. Abnormal values can be observed in the graph, for instance, the relative density dropped from 75 to 100 mA mm^{-2} for the dwell times of both 30 and 60 s. The deviation is mainly due to the divergence of the temperatures of the samples at the same current density. During flash sintering experiments, the dissipated power density has been found to vary for different experiments even using the same
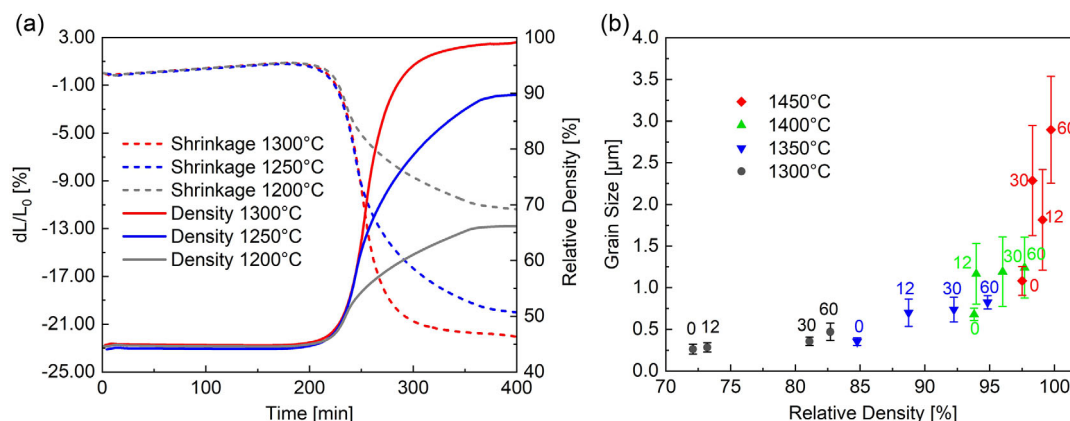
Figure 1. Experimental results for conventional sintering: a) sintering shrinkage and RD as a function of time; b) sintering trajectory at different sintering temperatures and with different dwell times. The dwell time (min) is indicated by the number around each colored dot.
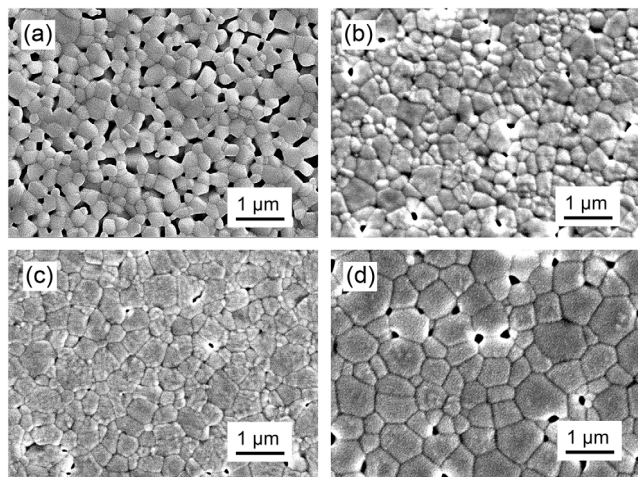

Figure 2. Microstructural evolution of 8YSZ samples conventionally sintered at 1350 °C for a) 0 min, b) 12 min, c) 30 min, and d) 60 min.

The exact reason for the deviation is unclear but can likely be attributed to the electrical contact resistance and the systematic error of the device and the setup. Therefore, the temperature rather than the current density is of interest for the analysis of the densification behavior. In the following analysis, the temperatures of the gauge sections of the dog-bone samples during the isothermal period were extracted from the simulation and averaged, which were subsequently adopted as the sintering temperature for each flash sintering experiment. The plot of RD as a function of temperature can be then constructed in Figure 3b. It can be seen that the deviation of the relative densities at $100\,\mathrm{mA\,mm^{-2}}$ for 30 and 60 s in Figure 3a is mitigated in Figure 3b. The diagram reveals that at around 1400 °C, the maximum RD of around 95% can be achieved within 15 s by flash sintering. This demonstrates that flash sintering can significantly accelerate the sintering process and achieve high densification of 8YSZ samples.

To characterize the grain size distribution in the flash sintered dog-bone samples, the microstructure at three different positions (position A, B, and C) was analyzed, as shown in **Figure 4**a. The measured mean grain sizes of the sample flash sintered at 50, 100, and $125\,\mathrm{mA\,mm^{-2}}$ for 30 s were plotted for each position in Figure 4c. The figure indicates a gradual decrease of grain size

current density, resulting in the variation of simulated temperatures (around 100 °C at high current densities) of the sample.
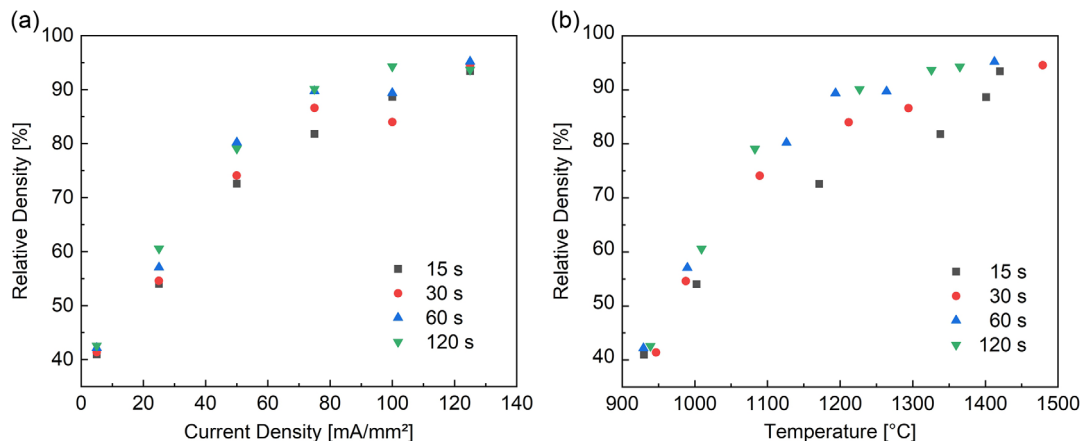

Figure 3. RD of flash sintered samples: a) RD as a function of current density; b) RD as a function of temperature.
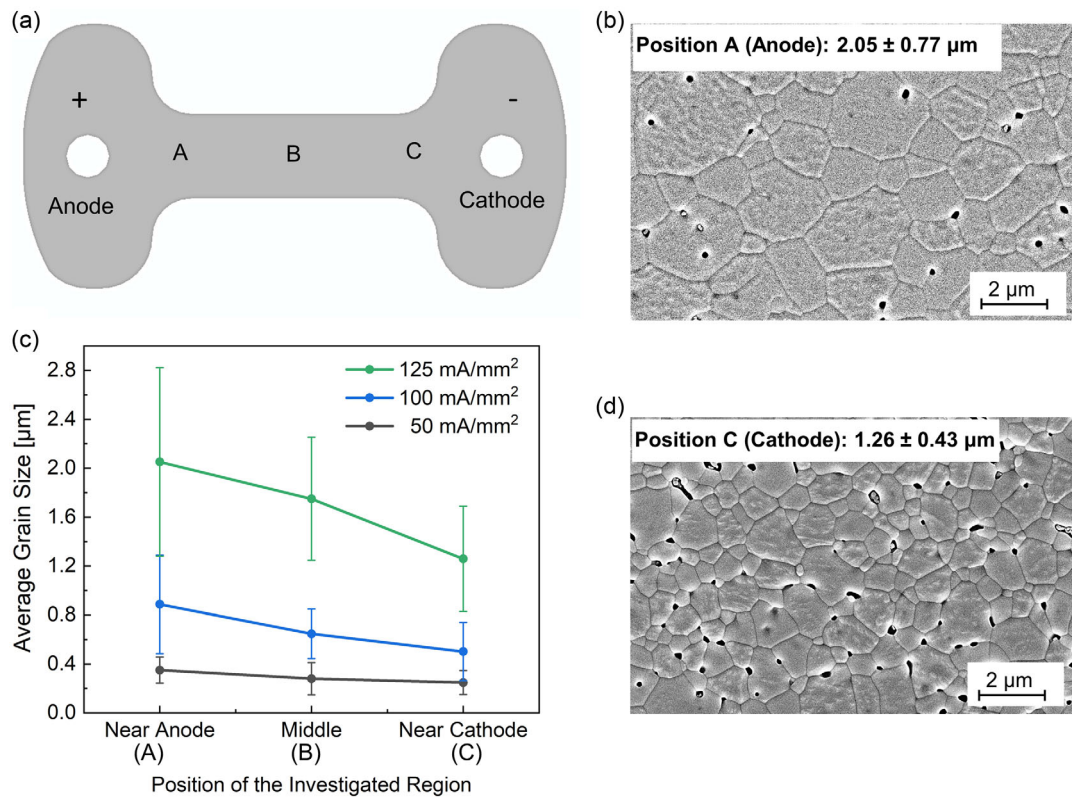
2201744 (5 of 14)

Figure 4. Grain size analysis for flash sintering: a) schematic representation of the measured positions of the gauge section of dog-bone shaped samples; b) microstructure at position A (near anode) of the sample flash sintered at 125 mA mm^{-2} for 30 s; c) grain sizes at position A, B, and C (corresponding to the positions on the dog-bone sample) at different current densities for the dwell time of 30 s; d) microstructure at position C (near cathode) of the sample flash sintered at 125 mA mm^{-2} for 30 s.

from the position near the anode side to that near the cathode side. Although the grain sizes are almost the same at different positions for the sample sintered at 50 mA mm^{-2}, the gradient enlarges with increasing current densities.

The micrographs at the positions close to the anode side (position A) and the cathode side (position C) of the sample flash sintered at 125 mA mm^{-2} for 30 s are shown in Figure 4b,d. The sample has a relative density of 95% and the grain size varies from 1.26 to 2.05 µm from the cathode side to the anode side. They are comparable to the grain sizes of conventional sintered samples at similar densities. For example, the sample conventionally sintered at 1400 °C for 30 min has a RD of 96% and a grain size of 1.63 µm. The grain sizes of the flash sintered 8YSZ samples align also well with the sintering trajectory of conventionally sintered 8YSZ samples.

4.1.2. Characterization of Densification

As there is only minor grain growth for the samples with a RD below 92%, constant grain sizes were assumed. Only the dilatometry experimental data of the RD smaller than 92% were utilized for the characterization of the densification behavior and the determination of exponential parameters for densification. For the calculation of densification, considering the case of pressure-less sintering with isotropic shrinkage, the strain rate can be formulated as Equation (6). With the

substitution of σ_s, η, and f, Equation (7) can be then obtained. To determine the exponent constant m (Equation (8)), Equation (7) was rewritten as the double logarithmic form given in Equation (9), where K_1 and K_2 are constants. By keeping the temperature T invariable and assuming a constant grain size G in our case, the left-hand side of Equation (9) against $\ln \rho$ can be plotted.

$$\dot{\varepsilon}_{kk} = -\frac{\dot{\rho}}{\rho} = \frac{1}{2\eta} \cdot \frac{1}{\rho^{2n-1}} \cdot \frac{2\sigma_s}{9f^2} \tag{6}$$

$$-\frac{\dot{\rho}}{\rho} = \frac{K_1}{C_{s1} T \exp\left(\frac{Q_d}{RT}\right) G} \cdot \rho^m \cdot (1-\rho)^{\frac{2}{3}} \tag{7}$$

$$m = N_S - 2n + \frac{4}{3} \tag{8}$$

$$\ln\left[\frac{\dot{\rho}}{\rho} \cdot \frac{1}{(1-\rho)^{\frac{2}{3}}}\right] = m \ln \rho + K_2 \tag{9}$$

$$\ln\left[T \cdot \frac{\dot{\rho}}{\rho} \cdot \frac{1}{\rho^m (1-\rho)^{\frac{2}{3}}}\right] = -\frac{Q_d}{RT} + K_3 \tag{10}$$

The double logarithmic plots for the dilatometry sintering at the temperatures of 1200, 1250, and 1300 °C are shown in **Figure 5**a. The results showed a linear feature and were fitted
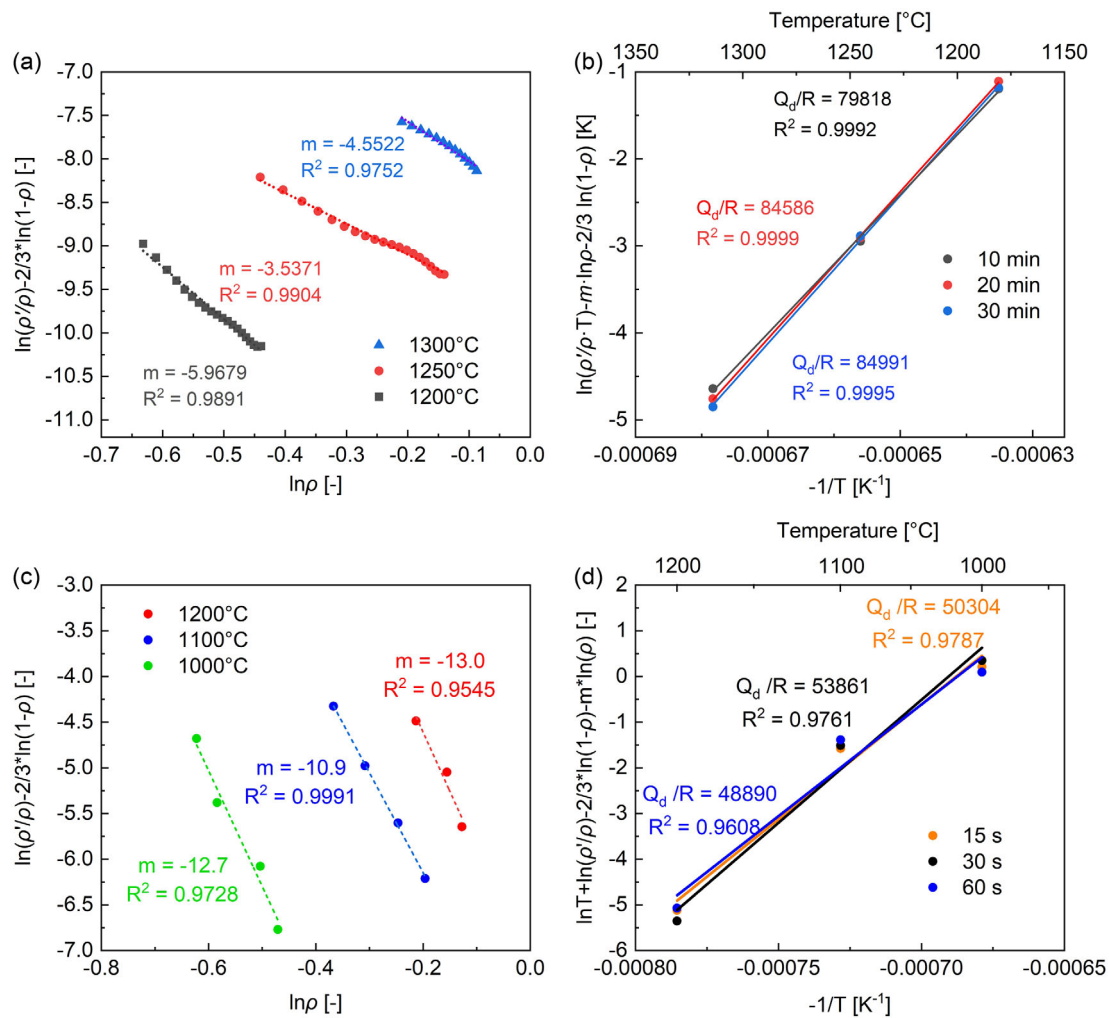
Figure 5. Parameter identification for densification: determination of parameter m for a) conventional sintering and c) flash sintering; determination of apparent activation energy of densification Q_d for b) conventional sintering and d) flash sintering.

by a linear function with a slope representing the parameter m. The average value of m was calculated to be -4.69 ± 1.00. After the calculation of exponential parameters, the apparent activation energy for densification Q_d was determined. Equation (7) was rewritten in the logarithmic form as shown in Equation (10). The left-hand side of the equation is plotted as a function of $-1/T$ in an Arrhenius plot (Figure 5b); the dwell times of 10, 20, and 30 min were chosen for the curves to ensure that the RD is below 92%. From the slopes of the curves, the average activation energy for densification can be obtained as $691 \pm 20 \, \text{kJ mol}^{-1}$.

The same strategy was adopted to identify the exponential parameters and the activation energy for densification for flash sintering. Unlike the dilatometry sintering experiments, the in situ shrinkage in the isothermal condition was unable to be recorded by flash sintering experiments. Therefore, interrupted isothermal experiments were designed to determine a densification curve as a function of the dwell time, from which the densification rate can be derived. However, the isothermal condition is hard to fulfill for different experiments even using the same current density. It can be seen from Figure 3 that a scatter of the

temperature exists for the same current density. Although the deviation is not that large, a fitting strategy was still employed for a more accurate parameter identification process. Based on the data from Figure 3b, density curves were fitted for each dwell time (Figure S1, Supporting Information). The density values at 1000, 1100, and 1200 °C are read from the fitted curves and extracted for the identification process. To determine the densification rate, the extracted relative densities were plotted against dwell time for 1000, 1100, and 1200 °C (Figure S2, Supporting Information). Subsequently, the parameter m and the apparent activation energy for densification Q_d were determined using the same way as for the conventional sintering. The linear regression plots are shown in Figure 5c,d. The average value of m was calculated to be -12.19 ± 0.90, and the activation energy Q_d was $424 \pm 17 \, \text{kJ mol}^{-1}$.

4.1.3. Characterization of Grain Growth

The measured grain sizes for conventional isothermal sintering experiments were plotted as a function of the dwell time in
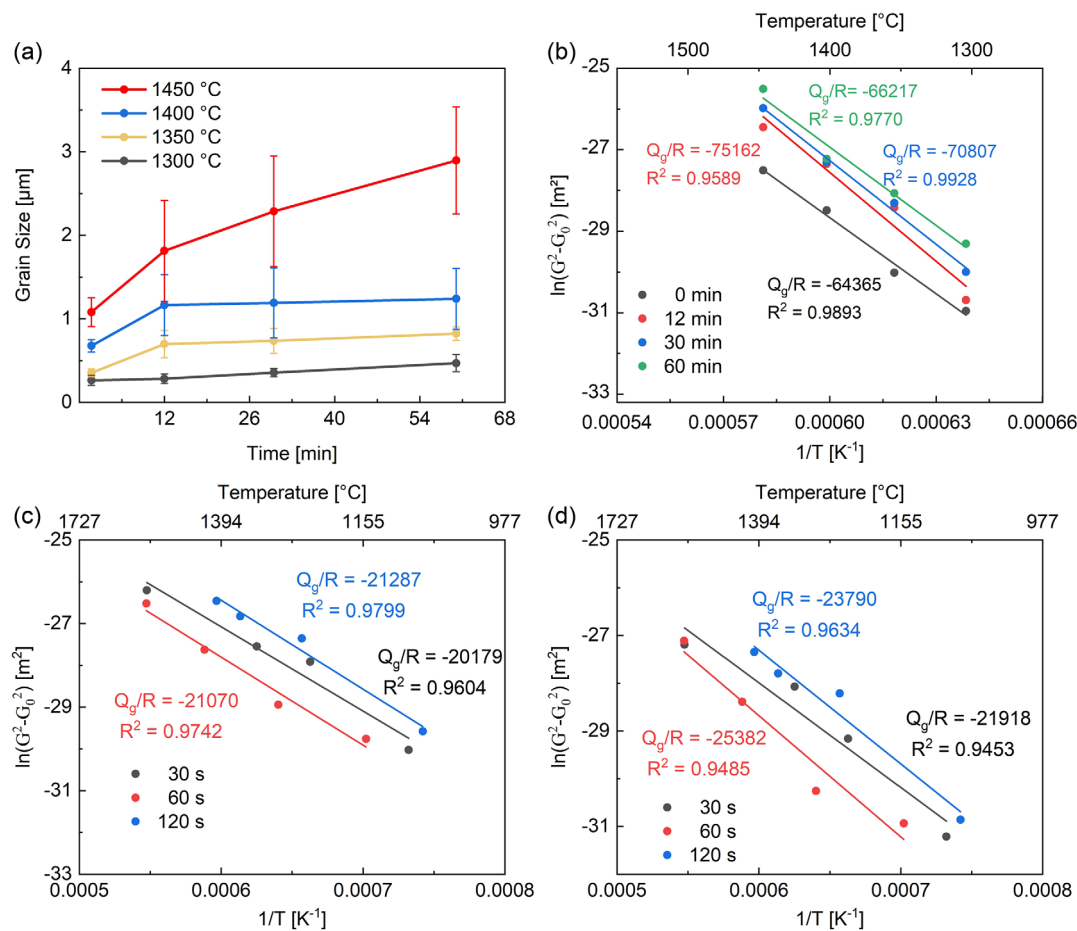
2201744 (7 of 14)

Figure 6. Parameter identification for grain growth: a) grain growth during conventional isothermal sintering at temperatures from 1300 to 1450 °C; b) determination of activation energy Q_g for grain growth for conventional sintering; c) determination of activation energy Q_g near the anode side of the sample during flash sintering; d) determination of activation energy Q_g near the cathode side of the sample during flash sintering.

Figure 6a. It shows that for the given dwell times, significant grain growth only occurred at a temperature above 1300 °C. Using the data from Figure 6a and rewriting Equation (5) to (11), linear regression plots were constructed as shown in Figure 6b. The value of grain growth exponent p was taken as 2 according to the literature[61] for 8YSZ.

$$\ln(G^p - G_0^p) = -\frac{Q_g}{RT} + \ln K_0 + \ln t \tag{11}$$

The activation energy Q_g can be determined by the slope of the fitted linear curves in Figure 6b. The average value for the four different temperatures was calculated to be $575 \pm 30\,\text{kJ mol}^{-1}$.

For flash sintering, different activation energies for grain growth were assumed at different positions of the dog-bone sample due to the electrical polarity. Therefore, the aforementioned parameter identification method was used to determine Q_g at three different positions of the dog-bone samples, namely, near the anode, in the middle, and near the cathode, which are labeled as positions A, B, and C in Figure 4a. A similar approach to the current work has been utilized to model the asymmetrical microstructure during field-assisted sintering (FAST/SPS) of GDC.[20] The temperatures were

extracted from the simulation models at each corresponding position on the dog-bone sample for the analysis. The linear regression plots are shown in Figure 6c,d for position A (anode) and C (cathode). The plot for position B (middle) is given in Figure S3, Supporting Information. The average activation energies of 173 ± 5, 189 ± 12, and $197 \pm 14\,\text{kJ mol}^{-1}$ were obtained for the anode, middle, and the cathode regions, respectively.

4.2. Simulation Results

4.2.1. Onset Temperature of Flash Sintering

The onset temperature of flash sintering, which is signaled by a nonlinear rise in electrical conductivity and a surge in power dissipation, has been found to be inversely related to the applied electric field.[62,63] As mentioned in Section 3.1, the convection coefficient in the finite element model was calibrated by comparing the flash-onset temperature between the numerical results and the experimental data from the literature.[51] A wide range of electric field (from 100 to 4000 V cm^{-1}) was applied in the simulation; thereafter, the temperature profiles of the gauge sections of the dog-bone samples were extracted and averaged after the

simulation. By plotting the temperature–time evolution curves, the flash-onset temperature can be determined by the point, where the abrupt increase of temperature occurs. Simulation results show that the onset temperature decreases with increasing electric field. By fitting the results with experimental data, the parameter of convection coefficient was calibrated to be 34 W m^{-2} K^{-1}. The change of onset temperature with respect to electric field is plotted in **Figure 7** for both experiment and simulation. The figure shows a very good agreement between the numerical and experimental results. In addition, the simulation with the electric fields higher than 4000 V cm^{-1} was also conducted, and the results show a barely change of the onset temperature, which indicates that a lower bound of the onset temperature is already reached at 4000 V cm^{-1}. This observation further confirms the hypothesis of the role of Debye temperature on the onset temperature of flash sintering[64] by using the electric field that can hardly be realized in experiments.
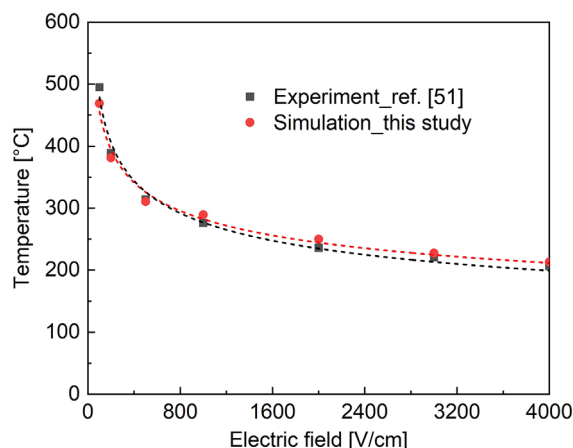

Figure 7. Comparison of simulation results and experimental values from ref. [51] of the flash-onset temperatures of 8YSZ with respect to different electric fields.
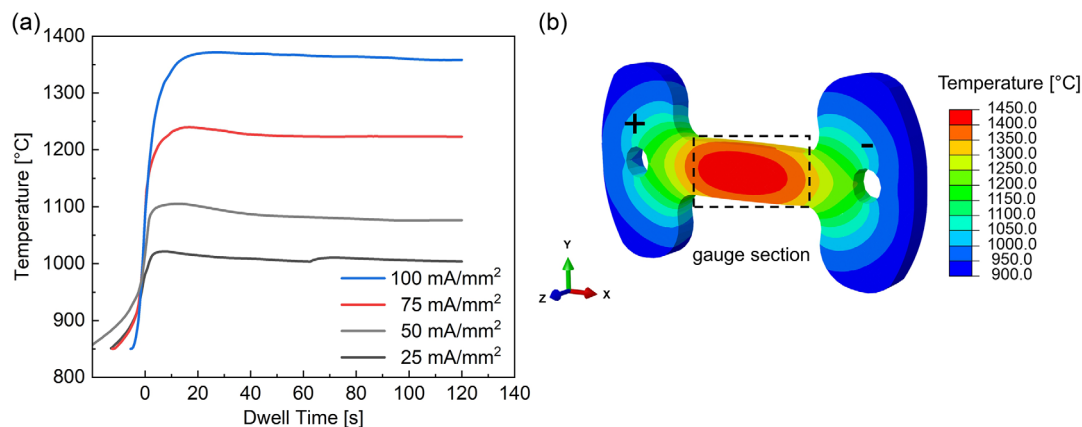
4.2.2. Temperature Distribution during Flash Sintering

To study the densification and grain growth during flash sintering, the temperature distribution in the sample must be first investigated by FEM. The temperature evolution of the sample was studied by extracting the average temperature of the gauge sections of the dog-bone samples from the simulation results. The evolution of the average temperature for the flash sintering at the current densities of 25, 50, 75, and 100 mA mm^{-2} with the dwell time of 120 s is shown in **Figure 8**a. The curves show that it only takes a few seconds to heat the sample from 850 °C to the maximum temperatures after the onset of flash sintering. Then the temperature stabilizes at the current-controlled period. Figure 8b demonstrates the temperature distribution in the dog-bone sample flash sintered at 100 mA mm^{-2} for 120 s. To show the reached maximum temperature on the gauge section of the sample, the model was cut along the xy-symmetry plane. The center of the sample has the highest temperature which decreases outward due to the thermal conduction and the radiation of the sample to the environment. A temperature gradient of around 150 °C was observed for the sample flash sintered at 100 mA mm^{-2} with 120 s. However, it was found from the simulation results that the temperature gradient decreases with a smaller current density. At a current density of 25 mA mm^{-2}, the temperature difference within the gauge section is only around 30 °C.

Figure 8b demonstrates a symmetrical temperature distribution for the flash sintered dog-bone sample. Some early studies[22,25,65] on flash sintering of YSZ indicate an electrochemical reduction of the material at the cathode side, which could reduce the electrical resistance of the material near the cathode, and thus lead to less heat dissipation at the cathode side and overheating at the anode side. In our study, the effect of electrochemical reduction was not initially considered in the model due to the difficulty in experimentally measuring the in situ local conductivity of the dog-bone samples. Additionally, Biesuz et al.[65] found that for the flash sintering of 8YSZ in "good contact" mode, where the Pt paste instead of Pt wire was used on the contact surface, the reduction of the cathode was much less evident and the temperature distribution in the sample was symmetrical. In

Figure 8. Temperature simulation during flash sintering: a) mean temperature evolution for 25, 50, 75, and 100 mA mm^{-2} with the dwell time of 120 s; b) temperature gradient in the dog-bone sample sintered at 100 mA mm^{-2} for 120 s and cut along its xy-symmetry plane.

the present work, a generous amount of Pt paste was applied between the sample holes and the electrodes to minimize the contact resistance. Therefore, a symmetrical temperature is assumed for this study. Further discussion of the effect of electrochemical reduction is given in Section 5.

4.2.3. Densification and Grain Growth

Upon the obtained constitutive parameters and the prediction of the temperature, the densification and grain growth behavior were also simulated for both conventional and flash sintering. For the implementation of grain growth model for flash sintering, the experimentally determined activation energy and the fitted pre-exponential parameters were adopted individually at the anode, middle, and cathode regions. The identification process of the activation energy was explained in Section 4.1.3. The grain growth parameters for the intermediate and outermost regions were determined using a linear interpolation method and were defined in the subroutine. The simulated relative densities in the gauge sections of the dog-bone samples were extracted and averaged. As for the grain size, the results were extracted at the anode (A), middle (B), and cathode (C) regions on its xy-symmetry plane. For conventional sintering, the temperature is

homogenous across the sample; thus, no specific requirement is needed for the evaluation of the results. In the following, the numerical results for both sintering techniques were compared with the experimental data, which are shown in **Figure 9**. In general, a good agreement between numerical and experimental data is achieved for both densification and grain growth. Relatively large deviation appears for flash sintering, which can be attributed to the difficulty of maintaining consistency in measuring density and grain size for the same gauge length/position of the dog-bone samples.

Furthermore, the density and grain size distributions are demonstrated for the dog-bone sample flash sintered at 100 mA mm^{-2} for 120 s in **Figure 10**. Figure 10a shows a density gradient that decreases from the cathode side (right) to the anode side (left), which might be highly related to the microstructural asymmetry depicted in Figure 10b. The larger grain sizes at the anode side can suppress further densification and lead to a smaller density than at the cathode side.

5. Discussion

With the aid of simulation, flash sintering can be compared with conventional sintering at similar sintering temperatures. To
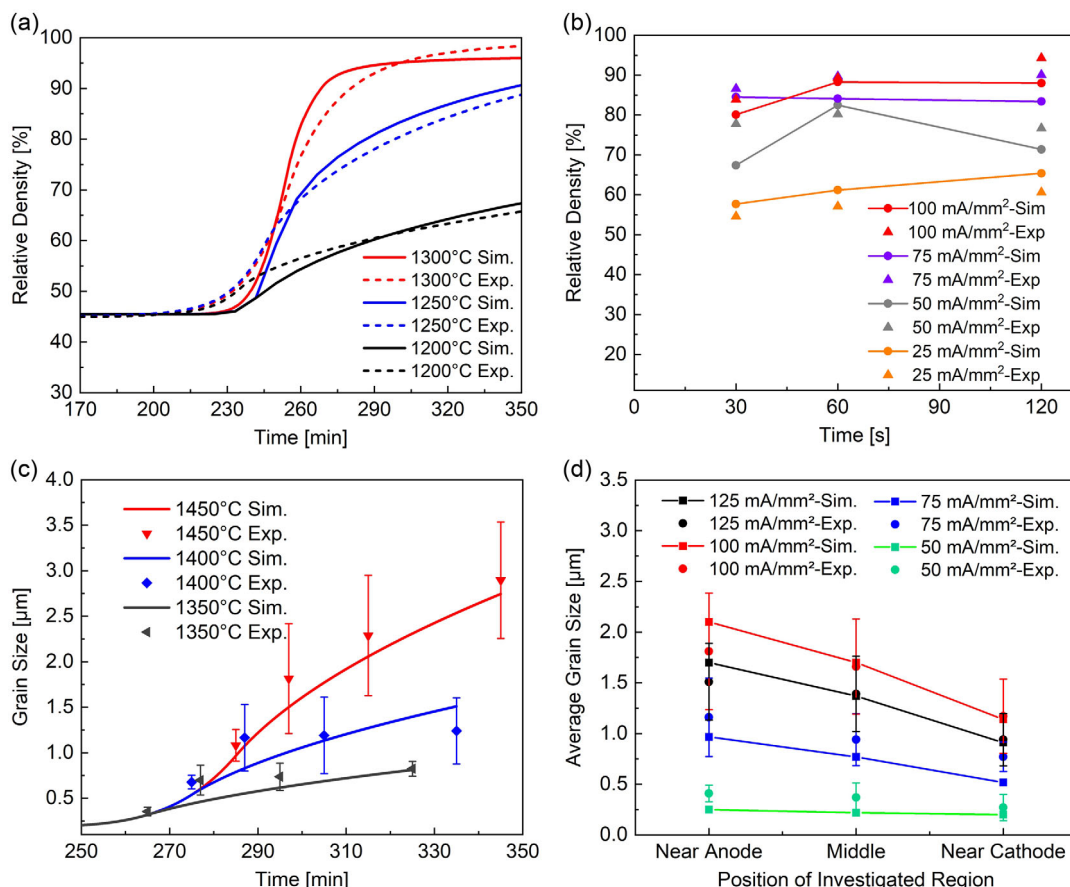

Figure 9. Experimental and simulation results of a) densification of conventional sintering at 1200, 1250, and 1300 °C for 2 h; b) densification of flash sintering at 25, 50, 75, and 100 mA mm^{-2} at the dwell time of 30, 60, and 120 s; c) grain growth of conventional sintering at 1350, 1400, and 1450 °C for 0, 12, 30, and 60 min; and d) grain growth of flash sintering at 25, 75, 100, and 125 mA mm^{-2} for 120 s.
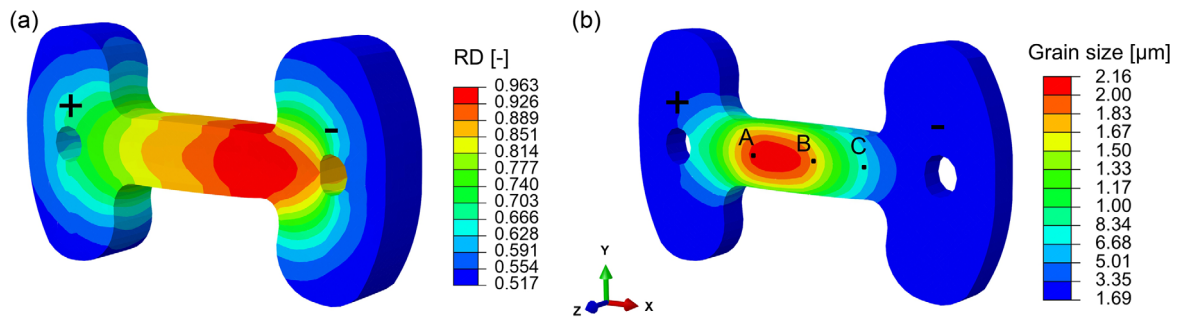
Figure 10. Simulation results of flash sintered samples at 100 mA mm^{-2} for 120 s: a) density distribution in the entire dog-bone sample; b) grain size distribution in the half of dog-bone sample cut along its xy-symmetry plane; A, B, and C indicate the positions where grain sizes were measured and analyzed for the anode, the center, and the cathode, respectively.

Table 2. Comparison of conventional sintering and flash sintering at similar sintering temperatures.

Conventional sintering				Flash sintering			
Temp. [°C]	Dwell time [s]	Heating rate [K min^{-1}]	RD [%]	Temp. [°C]	Dwell time [s]	Heating rate [K min^{-1}]	RD [%]
1200	60	5	52.9	1171	15	3012	72.6
1300	60	5	71.7	1294	30	2892	86.6
1350	720	5	88.7	1326	120	1393	93.7

study the effect of the heating rate on different sintering stages, three temperature ranges were chosen for comparison; the results of the selected simulations are shown in **Table 2**. It can be seen from the table that flash sintering, compared to conventional sintering, is able to achieve higher densification at relatively lower sintering temperatures and with shorter dwell times in all three cases. This reveals that the rapid densification during flash sintering of 8YSZ is not a result of an extremely high temperature. As the electric field has been found not to be the dominating factor enabling the fast densification in flash sintering of ZnO,[30] 3YSZ,[12,34] and 8YSZ,[24] it is then assumed that Joule heating is the main reason for this extremely fast densification in the current study. Hence, the different sintering behavior between conventional and flash sintering can be attributed to the heating rate. Table 2 also shows that flash sintering can reach a heating rate of 3000 K min^{-1}, which is significantly higher than 5 K min^{-1} for the conventional sintering. High heating rate is believed to be able to suppress surface diffusion processes that do not contribute to densification.[66] Consequently, the ceramic samples can quickly reach high temperatures where grain boundary diffusion dominates the mass transport during sintering.

An altered mass transport theory for flash sintering is also implied by the different apparent activation energies of densification. The calculated activation energy Q_d for conventional sintering is 691 ± 20 kJ mol^{-1}, which is consistent with the literature value of 688–757 kJ mol^{-1} for 8YSZ,[67–69] whereas flash sintering has a much smaller value of 424 ± 17 kJ mol^{-1}. The ability of flash sintering to reduce the activation energy for densification was also reported on uranium dioxide (UO$_2$), where the apparent activation energy was decreased from 380 to 108 kJ mol^{-1}.[70] Additionally, the reduction of the apparent activation energy for sintering was also observed in other sintering

techniques with high heating rate, such as FAST/SPS,[70,71] microwave sintering,[72] and UHS.[35,73] Although different sintering methods use different sintering aids (pressure, electric field, electromagnetic field, etc.), their common feature, ultrahigh heating rate, seems to be one of the major factors for changing the fundamental mass transport mechanism during sintering. It has been indicated that surface diffusion normally increases the apparent activation energy for densification.[74] This supports the theory that high heating rate can suppress surface diffusion, thereby decreasing the activation energy and facilitating densification.

Although with much shorter sintering times, flash sintering of 8YSZ did not produce a finer grain size than conventional sintering. In addition, a longer dwell time of flash sintering can lead to an even larger grain size than conventional sintering. For instance, for the samples with a RD of around 90%, the sample flash sintered at 75 mA mm^{-2} for 120 s has an average grain size of 0.96 μm, compared to 0.70 μm of conventional sintered sample (1350 °C for 12 min). Therefore, the grain growth behavior during flash sintering is not a factor of the acceleration of densification. On the contrary, the relatively faster grain growth seems to hinder further densification of flash sintered samples. This explains why the highest RD reached by flash sintering is only 95% and a long dwell time was not able to further increase the density. In contrast, almost full density can be achieved with sufficient holding time by conventional sintering. The influence of grain size on densification was also indicated by the simulation results (Figure 10), where a locally large grain size corresponds to a locally small density at the same temperature.

Microstructure characterization shows the largest grain sizes on the anode side of the 8YSZ samples after flash sintering (Figure 4c), which was also reported by Bhandari et al.[24] However, such observation of anode-favored grain growth is
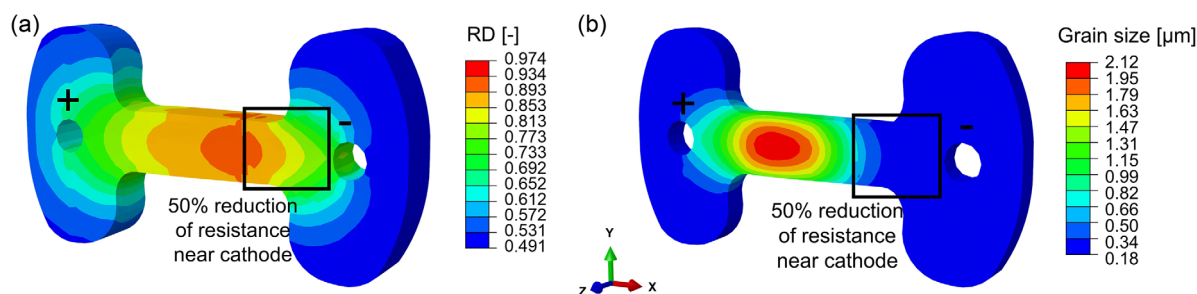
Figure 11. Simulation results of a flash sintered sample at 100 mA mm^{-2} for 120 s applying the partial reduction of the electrical resistivity near the cathode side: a) density distribution in the entire dog bone sample and b) grain size distribution in the half of dog-bone sample cut along its *xy*-symmetry plane.

in contrast to some previous studies on both 3YSZ and 8YSZ materials,[22,25] which exhibited much larger grain sizes at the cathode side than at the anode side. This was attributed to the electrochemical reduction of the material at the cathode. Such reduction can lower the migration barrier for diffusion and at the same time increase the grain boundary mobility.[22,25] As for the work of Bhandari et al.,[24] the faster grain growth at the anode side was explained by the temperature gradient induced by electrochemical reduction. Another observation of abnormal grain growth at the anode was reported on ZnO by Zhang et al.[18] In their work, the microstructural asymmetry was attributed to the formation of cation vacancies at the anode due to the local accumulation of free electrons. The increase of cation vacancies could lead to a decrease of activation energy of grain growth. The contrary findings of microstructural asymmetry during flash sintering imply that for different materials and different sintering processes (for instance current density and holding time), flash sintering may induce different grain growth enhancement mechanisms.

In this study, the theory of the accumulation of defects at the anode is adopted to account for the abnormal grain growth near the anode of the dog-bone sample. The activation energy for grain growth was calculated individually at the anode, the center, and the cathode regions. The results show a decrease in activation energy from the cathode (197 ± 14 kJ mol^{-1}) to the anode (173 ± 5 kJ mol^{-1}), which corresponds to a higher grain boundary mobility at the anode and thus a larger grain size compared to the cathode. The simulation results also show a decrease of grain size from the anode to the cathode side (Figure 10b), while the local relative density shows an inverse gradient (Figure 10a). However, considering the possible electrochemical reduction near the cathode side starting before the onset of flash, the simulated density distribution might not represent that of the real sample. A partial chemical reduction at the cathode can lead to the decrease of electrical resistance, thus less Joule heating and less densification near the cathode side. To study the influence of electrochemical reduction on the local density, a case study was conducted by assigning the cathode region (marked with black square in **Figure 11**), a smaller electrical resistivity in the modeling. Figure 11 shows the simulation results obtained by decreasing the electrical resistivity of 50% at the cathode region for the whole flash process. By comparing Figure 10 and 11, it can be concluded that a partial reduction near the cathode side delivers a more symmetrical density distribution, whereas the grain size distribution is scarcely influenced.

6. Summary

In this work, flash sintering of 8YSZ has been systematically studied both experimentally and numerically. The results were compared with that of conventional sintering to identify important influencing factors. Additionally, the densification and grain growth kinetics were also analyzed correspondingly. The drawn conclusions are in the following: 1) Flash sintering can be used to densify the green samples of 8YSZ to a RD of 95% at 125 mA mm^{-2} within 30 s. Based on the simulation results of the thermal history and the comparison with conventional sintering, the rapid densification was attributed to the ultrahigh heating rate (2000–3000 K min^{-1}) rather than the high maximum temperature. A decrease of the apparent activation energy for densification in flash sintering indicates an enhanced mass transport, which is plausibly induced by ultrahigh heating rate that suppresses the surface diffusion and enhances the grain boundary diffusion. 2) Flash onset temperature has been simulated at different electric fields, and an inverse relationship between the onset temperature and the electric field was obtained, which matches the experimental observation of 8YSZ. This numerical reproduction confirms the theory of Debye temperature as the lower boundary of the flash onset temperature of 8YSZ. 3) Microstructural asymmetry caused by electrical polarity during flash sintering of 8YSZ was studied experimentally and numerically. Larger grain sizes were observed at the anode side compared to the cathode side, which corresponds to a smaller activation energy for grain growth at the anode side. With the separately implemented activation energies at different positions, inhomogeneous grain growth behavior was successfully simulated. Furthermore, the densification during flash sintering was also predicted by simulation, which reveals a good agreement with the experimental data. 4) Simulation models with and without the consideration of the factor of electrochemical reduction show different density distributions in the dog-bone samples. A more accurate description of the electrochemical reduction in the model needs to be given in the future by real measurement of the local electrical conductivity in the dog-bone samples during flash sintering.

Supporting Information

Supporting Information is available from the Wiley Online Library or from the author.

Conflict of Interest

The authors declare no conflict of interest.

Data Availability Statement

The data that support the findings of this study are available from the corresponding author upon reasonable request.

[1] M. Cologna, B. Rashkova, R. Raj, *J. Am. Ceram. Soc.* **2010**, *93*, 3556.
[2] R. Raj, M. Cologna, A. L. G. Prette, V. Sglavo, US20130085055A1 **2013**.
[3] R. I. Todd, E. Zapata-Solvas, R. S. Bonilla, T. Sneddon, P. R. Wilshaw, *J. Eur. Ceram. Soc.* **2015**, *35*, 1865.
[4] S. Grasso, Y. Sakka, N. Rendtorff, C. Hu, G. Maizza, H. Borodianska, O. Vasylkiv, *J. Ceram. Soc. Jpn.* **2011**, *119*, 144.
[5] J. G. P. Da Silva, H. A. Al-Qureshi, F. Keil, R. Janssen, *J. Eur. Ceram. Soc.* **2016**, *36*, 1261.
[6] Y. Zhang, J. Luo, *Scr. Mater.* **2015**, *106*, 26.
[7] Y. Dong, I.-W. Chen, *J. Am. Ceram. Soc.* **2015**, *98*, 3624.
[8] R. Chaim, *Materials* **2016**, *9*, 280.
[9] J.-C. M'Peko, J. S. C. Francis, R. Raj, *J. Am. Ceram. Soc.* **2013**, *96*, 3760.
[10] J. Narayan, *Scr. Mater.* **2013**, *69*, 107.
[11] E. Zapata-Solvas, D. Gómez-García, A. Domínguez-Rodríguez, R. I. Todd, *Sci. Rep.* **2015**, *5*, 8513.
[12] W. Ji, B. Parker, S. Falco, J. Y. Zhang, Z. Y. Fu, R. I. Todd, *J. Eur. Ceram. Soc.* **2017**, *37*, 2547.
[13] M. Biesuz, V. M. Sglavo, *Scr. Mater.* **2018**, *150*, 82.
[14] T. P. Mishra, R. R. I. Neto, G. Speranza, A. Quaranta, V. M. Sglavo, R. Raj, O. Guillon, M. Bram, M. Biesuz, *Scr. Mater.* **2020**, *179*, 55.
[15] M. Jongmanns, R. Raj, D. E. Wolf, *New J. Phys.* **2018**, *20*, 93013.
[16] J. S. Francis, M. Cologna, R. Raj, *J. Eur. Ceram. Soc.* **2012**, *32*, 3129.
[17] C. Schmerbauch, J. Gonzalez-Julian, R. Röder, C. Ronning, O. Guillon, *J. Am. Ceram. Soc.* **2014**, *97*, 1728.
[18] Y. Zhang, J.-I. Jung, J. Luo, *Acta Mater.* **2015**, *94*, 87.
[19] J.-W. Jeong, J.-H. Han, D.-Y. Kim, *J. Am. Ceram. Soc.* **2000**, *83*, 915.
[20] S. K. Sistla, T. P. Mishra, Y. Deng, A. Kaletsch, M. Bram, C. Broeckmann, *J. Am. Ceram. Soc.* **2021**, *104*, 1978.
[21] T. P. Mishra, R. R. I. Neto, R. Raj, O. Guillon, M. Bram, *Acta Mater.* **2020**, *189*, 145.
[22] S.-W. Kim, S. G. Kim, J.-I. Jung, S.-J. L. Kang, I.-W. Chen, *J. Am. Ceram. Soc.* **2011**, *94*, 4231.
[23] W. Xu, A. Maksymenko, S. Hasan, J. J. Meléndez, E. Olevsky, *Acta Mater.* **2021**, *206*, 116596.

[24] S. Bhandari, T. P. Mishra, O. Guillon, D. Yadav, M. Bram, *Scr. Mater.* **2022**, *211*, 114508.
[25] W. Qin, H. Majidi, J. Yun, K. van Benthem, *J. Am. Ceram. Soc.* **2016**, *99*, 2253.
[26] C. Cao, R. Mücke, O. Guillon, *Acta Mater.* **2020**, *182*, 77.
[27] S. K. Jha, H. Charalambous, H. Wang, X. L. Phuah, C. Mead, J. Okasinski, H. Wang, T. Tsakalakos, *Ceram. Int.* **2018**, *44*, 15362.
[28] K. Vikrant, W. Rheinheimer, H. Sternlicht, M. Bäurer, R. E. García, *Acta Mater.* **2020**, *200*, 727.
[29] M. Biesuz, V. M. Sglavo, *J. Eur. Ceram. Soc.* **2019**, *39*, 115.
[30] Y. Zhang, J. Nie, J. M. Chan, J. Luo, *Acta Mater.* **2017**, *125*, 465.
[31] *Ultra-Rapid Sintering: Volume 16 Sintering and Heterogeneous Catalysis* (Ed: D. L. Johnson), Springer US, Boston, MA **1984**.
[32] D. L. Johnson, *J. Appl. Phys.* **1969**, *40*, 192.
[33] D. Lynn Johnson, W. B. Sanderson, E. L. Kemer, J. Knowlton, *MRS Proc.* **1983**, *24*, 273.
[34] W. Ji, J. Zhang, W. Wang, Z. Fu, R. I. Todd, *J. Eur. Ceram. Soc.* **2020**, *40*, 5829.
[35] C. Wang, W. Ping, Q. Bai, H. Cui, R. Hensleigh, R. Wang, A. H. Brozena, Z. Xu, J. Dai, Y. Pei, C. Zheng, G. Pastel, J. Gao, X. Wang, H. Wang, J.-C. Zhao, B. Yang, X. R. Zheng, J. Luo, Y. Mo, B. Dunn, L. Hu, *Science* **2020**, *368*, 521.
[36] T. P. Mishra, S. Wang, C. Lenser, D. Jennings, M. Kindelmann, W. Rheinheimer, C. Broeckmann, M. Bram, O. Guillon, *Acta Mater.* **2022**, *231*, 117918.
[37] R. Raj, *J. Eur. Ceram. Soc.* **2012**, *32*, 2293.
[38] P. Kumar M K, D. Yadav, J.-M. Lebrun, R. Raj, *J. Am. Ceram. Soc.* **2018**, *93*, 3556.
[39] J. G. Pereira da Silva, J.-M. Lebrun, H. A. Al-Qureshi, R. Janssen, R. Raj, *J. Am. Ceram. Soc.* **2015**, *98*, 3525.
[40] R. Serrazina, P. M. Vilarinho, A. M. Senos, L. Pereira, I. M. Reaney, J. S. Dean, *J. Eur. Ceram. Soc.* **2020**, *40*, 1205.
[41] Y. Li, R. Torchio, P. Falco, P. Alotto, Z. Huang, R. I. Todd, *J. Eur. Ceram. Soc.* **2021**, *41*, 6649.
[42] K. S. Arya, A. Eqbal, P. Rai, D. Yadav, T. Chakrabarti, *J. Am. Ceram. Soc.* **2022**, *105*, 6049.
[43] K. Maca, V. Pouchly, A. R. Boccaccini, *Sci. Sintering* **2008**, *40*, 117.
[44] M. Cologna, J. S. Francis, R. Raj, *J. Eur. Ceram. Soc.* **2011**, *31*, 2827.
[45] M. I. MENDELSON, *J. Am. Ceram. Soc.* **1969**, *52*, 443.
[46] Hibbitt, Karlsson and Sorensen, *ABAQUS 5.8 Theory Manual*, Hibbitt, Karlsson & Sorensen Inc., Pawtucket, USA **1998**.
[47] A. Zavaliangos, J. Zhang, M. Krammer, J. R. Groza, *Mater. Sci. Eng., A* **2004**, *379*, 218.
[48] J. Zhang, Z. Wang, T. Jiang, L. Xie, C. Sui, R. Ren, J. Qiao, K. Sun, *Ceram. Int.* **2017**, *43*, 14037.
[49] H. Tanaka, S. Sawai, K. Morimoto, K. Hisano, *J. Therm. Anal. Calorim.* **2001**, *64*, 867.
[50] A. J. Wright, C. Huang, M. J. Walock, A. Ghoshal, M. Murugan, J. Luo, *J. Am. Ceram. Soc.* **2021**, *104*, 448.
[51] D. Yadav, R. Raj, *J. Am. Ceram. Soc.* **2017**, *100*, 5374.
[52] J. Zhang, C. Lenser, N. H. Menzler, O. Guillon, *Solid State Ionics* **2020**, *344*, 115138.
[53] V. V. Skorohod, *Rheological Basis of the Theory of Sintering*, Naukova Dumka, Kiev **1972**.
[54] E. A. Olevsky, *Mater. Sci. Eng.: R: Rep.* **1998**, *23*, 41.
[55] K. Shinagawa, *Comput. Mater. Sci.* **1999**, *13*, 276.
[56] K. Shinagawa, *JSME Int J., Ser. A* **1996**, *39*, 565.
[57] C. van Nguyen, S. K. Sistla, S. van Kempen, N. A. Giang, A. Bezold, C. Broeckmann, F. Lange, *J. Ceram. Soc. Jpn.* **2016**, *124*, 301.
[58] M. Renaux, D. Méresse, J. Pellé, A. Thuault, C. Morin, C. Nivot, C. Courtois, *J. Eur. Ceram. Soc.* **2021**, *41*, 6617.

[59] J. E. Burke, D. Turnbull, *Prog. Met. Phys.* **1952**, *3*, 220.

[60] M. Hillert, *Acta Metall.* **1965**, *13*, 227.

[61] X. Wang, A. Atkinson, *Acta Mater.* **2011**, *59*, 2514.

[62] S. K. Jha, R. Raj, *J. Am. Ceram. Soc.* **2014**, *97*, 527.

[63] R. Raj, *J. Am. Ceram. Soc.* **2016**, *99*, 3226.

[64] T. P. Mishra, V. Avila, R. R. I. Neto, M. Bram, O. Guillon, R. Raj, *Scr. Mater.* **2019**, *170*, 81.

[65] M. Biesuz, L. Pinter, T. Saunders, M. Reece, J. Binner, V. M. Sglavo, S. Grasso, *Materials* **2018**, *11*, 1214.

[66] D. L. Johnson, *J. Am. Ceram. Soc.* **1990**, *73*, 2576.

[67] B.-N. Kim, T. S. Suzuki, K. Morita, H. Yoshida, Y. SAKKA, H. Matsubara, *J. Eur. Ceram. Soc.* **2016**, *36*, 1269.

[68] K. Matsui, K. Tanaka, T. Yamakawa, M. Uehara, N. Enomoto, J. Hojo, *J. Am. Ceram. Soc.* **2007**, *90*, 443.

[69] G. Suárez, N. M. Rendtorff, A. N. Scian, E. F. Aglietti, *Ceram. Int.* **2013**, *39*, 261.

[70] R. R. Ingraci Neto, K. J. McClellan, D. D. Byler, E. Kardoulaki, *J. Nucl. Mater.* **2021**, *547*, 152780.

[71] O. Guillon, J. Langer, *J. Mater. Sci.* **2010**, *45*, 5191.

[72] M. A. Janney, H. D. Kimrey, *MRS Proc.* **1990**, *189*, 215.

[73] Y. Lin, N. Luo, E. Quattrocchi, F. Ciucci, J. Wu, M. Kermani, J. Dong, C. Hu, S. Grasso, *Ceram. Int.* **2021**, *47*, 21982.

[74] G. Sethi, S. J. Park, J. L. Johnson, R. M. German, *Int. J. Refract. Met. Hard Mater.* **2009**, *27*, 688.